New Phytologist

Research

Methods

Semiautomatic quantification of 3D Histone H3 phosphorylation signals during cell division in Arabidopsis root meristems

Adrienn Kelemen[1,2], Magalie Uyttewaal[1], Csaba Máthé[2], Philippe Andrey[1], David Bouchez[1] and Martine Pastuglia[1]

[1]Université Paris-Saclay, INRAE, AgroParisTech, Institut Jean-Pierre Bourgin for Plant Sciences (IJPB), Versailles, 78000, France; [2]Plant Cell and Developmental Biology Research Group, Department of Botany, Faculty of Science and Technology, University of Debrecen, Egyetem ter 1, Debrecen, H-4032, Hungary

Authors for correspondence:
Martine Pastuglia
Email: martine.pastuglia@inrae.fr

David Bouchez
Email: david.bouchez@inrae.fr

Received: *25 February 2025*
Accepted: *14 June 2025*

New Phytologist (2025)
doi: 10.1111/nph.70365

Key words: 3D image analysis, cell division, histone phosphorylation, PP2A, signal quantification.

Summary

- Posttranslational modification of histones during the cell cycle is a major process controlling many aspects of cell division. Among the variety of histone modifications, mitotic phosphorylation of histone H3 at serine 10 (H3S10ph) plays a crucial role, particularly in proper chromosome segregation. Here we aimed at precisely quantifying this phosphorylation dynamics during mitosis in plant cells in order to reveal molecular pathways involved in this process.
- We describe an analysis pipeline based on 3D image analysis that allows to semiautomatically quantify H3S10ph in mitotic Arabidopsis root cells. We also developed a new method for the compensation of signal attenuation in *Z*, based on measurement of objects of interest themselves.
- We show that this new attenuation correction method allows significant gains in accuracy and statistical power. Using this pipeline, we were able to reveal small H3S10ph differences between cells treated with hesperadin, an inhibitor of an H3S10ph kinase, or between Arabidopsis mutants affected in PP2A phosphatase activity.
- This tool opens new avenues to explore such regulatory pathways in plants, using the wealth of genetic materials available in Arabidopsis. It can also be applied to study other histone posttranslational modifications and more generally to any discrete 3D signals.

Introduction

Eukaryotic genomes are highly compacted and complexed with histones, basic packaging proteins able to neutralize the negatively charged sugar–phosphate backbone of the DNA molecule. During mitosis and meiosis, chromatin undergoes maximal condensation into chromosomes, a hallmark of eukaryotic cell division.

The basic repeating unit of chromatin is the nucleosome, which consists of 147 base pairs (bp) of DNA spiraling around an octamer core involving two molecules of each core histone (H2A, H2B, H3 and H4) (Luger *et al.*, 2012). Histones are globular proteins containing a histone-fold serving as both dimerization and DNA-binding domains and possess a 20–35 amino acid N-terminal basic extension that extends from the surface of the nucleosome. The synthesis and incorporation of so-called canonical histones in animals and plants are coupled to S-phase DNA synthesis, where they assemble into nucleosomes following the replication fork. On the contrary, histone variants are incorporated throughout the cell cycle, independently of DNA synthesis, and play a diversity of roles and functions (Talbert *et al.*, 2012).

As the major protein component of chromatin, histones are key determinants of the chromatin landscape. Histones, especially H3 and H4, routinely undergo extensive reversible posttranslational modifications (PTMs) such as phosphorylation, acetylation, methylation, ubiquitination, sumoylation, etc. The N-terminal histone tail is particularly subject to such modifications. The combination of histone posttranslational marks constitutes the 'histone code' that directly regulates accessibility of various proteins such as histone chaperones or other chromatin modifying and remodeling factors and inform on transcriptional properties (permissive vs repressive) (Sawicka & Seiser, 2012).

Among the variety of histone modifications, mitotic phosphorylation of histone H3 at serine 10 (H3S10ph) has been widely studied in many eukaryotic organisms (Sawicka & Seiser, 2012; Wang & Higgins, 2013), including plants (Zhang *et al.*, 2014). Several functions for this PTM have been proposed, related to chromosome condensation, recruitment or exclusion of chromatin modifiers, transcriptional activation, or cohesion of sister chromatids (Kaszás & Cande, 2000; Houben *et al.*, 2007; Sawicka & Seiser, 2012). In plants, this archetypal mitotic histone modification is minimal during interphase, is first observed

in early prophase, peaks in late prophase to metaphase and disappears with the decondensation of chromosomes at telophase, as shown in several species (Houben *et al.*, 1999; Manzanero *et al.*, 2002). Thanks to highly specific H3S10ph antibodies (Hendzel *et al.*, 1997), it was shown in many animal species that H3S10ph starts in the pericentromeric region and spreads throughout the chromosomes both in mitosis and meiosis. In plants, however, only the pericentromeric region is highly phosphorylated in mitosis and the second meiotic division, whereas chromosomes are phosphorylated along their whole length during the first meiotic division (Manzanero *et al.*, 2000; Gernand *et al.*, 2003).

In animal cells, the main kinase involved in H3S10ph is Aurora B, which is activated at mitotic entry and phosphorylates Ser10 and Ser28 on histone H3. All mitotic phosphosites of histone H3 (T3, S10 and S28) are then removed upon mitotic exit by the Repo-man/protein phosphatase 1 (PP1) (Gil & Vagnarelli, 2019). The balance between Aurora and PP1 was shown to be critical for the balance of H3 phosphorylation during mitosis in yeast and *Caenorhabditis elegans* and important for proper chromosome segregation (Hsu *et al.*, 2000).

In Arabidopsis, three Aurora homologs were identified (AtAUR1, AtAUR2 and AtAUR3). All have the ability to phosphorylate H3S10 *in vitro*, but during mitosis, only AtAUR3 displayed a localization dynamics similar to H3S10ph (Demidov *et al.*, 2005; Kawabe *et al.*, 2005). *In vitro* experiments using the Aurora inhibitor hesperadin inhibited the kinase activity of AtAUR3 toward both H3S10 and H3S28, and in tobacco BY-2 cells, hesperadin inhibited both mitotic H3S10ph and H3S28ph (Kurihara *et al.*, 2006). It was also shown that *in vitro*, H3S10ph is altered by methylation, acetylation or phosphorylation of neighboring amino acid residues, showing strong interactions between various PTMs of the H3 N-terminal tail (Demidov *et al.*, 2009).

The phosphatase activity responsible for removing H3S10ph at mitotic exit is not yet identified in plants. Cantharidin, a specific inhibitor of PP1 and PP2A protein phosphatases, strongly modifies the chromosomal distribution of H3S10ph, displacing its pericentromeric localization to the whole mitotic chromosome, resembling the distribution seen in the first meiotic division (Manzanero *et al.*, 2002). Likewise, microcystin-LR, a drug that inhibits both PP2A and PP1 activities, induces hyperphosphorylation of histone H3 at Ser10 in lateral root apical meristems of *Vicia faba* (Beyer *et al.*, 2012).

Despite these pioneering studies, the dynamics of H3S10ph in plant cell division is not known with precision, in particular, due to the absence of robust methods aimed at quantifying the *in vivo* levels of phosphorylated histones in time and space. In order to identify the molecular pathways involved in such phosphocontrol, we developed an image-based method to semiautomatically quantify H3S10ph levels in mitotic Arabidopsis root cells. Using whole-mount immunolocalization with a specific H3S10ph antibody (Hendzel *et al.*, 1997), we acquired 3D images of root tips, allowing us to dynamically assess H3S10ph during all mitotic phases in root cells. We designed a set of ImageJ/Fiji macros to automatically segment H3S10ph signals and measure their values in root mitotic nuclei. However, initial measurements revealed a strong signal attenuation with depth, precluding accurate signal quantification. Signal attenuation is indeed a well-known caveat in confocal *Z*-stack imaging mainly due to the scattering and absorption of both excitation and emitted light or photobleaching. We thus developed a robust estimation of signal attenuation with depth, based on the objects of interest themselves, allowing for subsequent correction of the confocal stack and a strongly improved quantification of the signal. As a proof of concept, we used this method to quantitatively evaluate the impact of hesperadin treatment (an Aurora kinase inhibitor) as well as the impact of mutations in phosphatase 2A subunits on the mitotic phosphorylation of Histone H3 in dividing Arabidopsis root cells.

Materials and Methods

Growth conditions and plant material

Arabidopsis thaliana L. seedlings were grown *in vitro* under long-day conditions (16 h in light : 8 h in dark regime, 21°C) on ½MS media. All mutants used in this study are in the Col0 background and have already been described: the *pp2aa* double mutants in Zhou *et al.* (2004), the *pp2ac3 pp2ac4* double mutant in Spinner *et al.* (2013), the *trm6 trm7 trm8* (*trm678*) triple mutant in Schaefer *et al.* (2017).

Hesperadin treatment

Three-day-old *in vitro* grown seedlings were transferred for 24 h to a ½MS media containing 1 μM or 5 μM hesperadin (375 680, stock solution at 50 mM in dimethy sulfoxide (DMSO; Sigma-Aldrich) or DMSO (0.02%) for the untreated control seedlings.

Whole-mount immunolocalization

Four-day-old Arabidopsis seedlings were fixed in 4% paraformaldehyde and 0.1% Triton X100 in MTSB ½ buffer (25 mM PIPES, 2.5 mM MgSO4, 2.5 mM ethylene glycol-bis(ő-aminoethyl ether)-N,N,N',N'-tetraacetic acid (EGTA), pH 6.9) for 1 h under vacuum, then rinsed in MTSB ½ for 10 min. Samples were then permeabilized in 100% Methanol for 15 min and rinsed in PBS buffer 1× (GAUPBS00-01, Eurobio Scientific, les Ulis, France) for 10 min. Cell walls were digested for 55 min in the digestion buffer (5 mM) MES pH 5, 0.02% Driselase (Driselase™ *Basidiomycetes* sp., D8037; Sigma-Aldrich, St Louis, MO, USA) and 0.015% Macerozyme (Macerozyme R-10; Yakult Pharmaceutical Industry Co., Tokyo, Japan). After rinsing in PBS for 10 min, samples were labeled overnight at 4°C with the B-5-1-2 mouse monoclonal anti-tubulin (T5168, dilution 1/2000; Sigma-Aldrich) and a rabbit polyclonal anti-H3S10ph antibody (ab5176, 1/2000, 0.5 μg ml^{-1}; Abcam limited, Cambridge, UK). The next day, tissues were washed for 20 min in PBS with 50 mM glycine and incubated overnight with 1/2000 dilutions of secondary antibodies (Alexa Fluor 555 goat

anti-mouse for the anti-tubulin antibody and Alexa Fluor 488 goat anti-rabbit for the anti-H3S10ph antibody, A-21422 and A-11008; Thermo Fischer Scientific, Waltham, MA, USA). Samples were then rinsed for 20 min in PBS with 50 mM glycine, stained for 30 min in 4',6-diamidino-2-phénylindole (DAPI) (4',6-diamidino-2-phenylindole, 0.01 mg ml^{-1} in PBS), and rinsed for 20 min in PBS. When TO-PRO-3 was used in addition to DAPI, samples were then stained in TO-PRO-3 (T3605, dilution 1/1000; Invitrogen, Carlsbad, CA, USA) for 30 min and rinsed for 20 min in PBS. Roots were mounted in the Vectashield® antifade mounting medium using a Secure-Seal™ Spacer (8 wells, 9 mm diameter, 0.12 mm deep) to prevent any deformation of the samples.

Image acquisition

Immunolocalized seedlings were viewed using an SP8 confocal laser microscope (Leica Microsystems, Wetzlar, Germany). For simultaneous detection of DAPI, microtubules, and H3S10ph signals, samples were excited, respectively, at 405, 488 or 561 nm, with emission bands of 420–446 nm, 495–540 nm or 570–620 nm, using photomultiplier tube (PMT) detectors for both DAPI and H3S10ph, and a hybrid detector for microtubules. All 3D stacks were acquired as 12-bit images to get a high dynamic range of the H3S10ph signal, ensuring that no pixel was saturated in this channel. Image acquisition was highly standardized: All 3D stacks were acquired using the same zoom, the same voxel size (350 nm × 350 nm × 350 nm) and the same settings. The H3S10ph signal was acquired with a PMT, using the same laser power, the same acousto-optic tunable filter (AOTF), the same PMT gain, no offset and a line average of 2 for all images. All genotypes and treatments to be compared were immunolocalized in the same experiments and imaged at the same time. An average of 7–8 roots per treatment or genotype were analyzed.

For simultaneous detection of DAPI, TO-PRO-3, H3S10ph and microtubules, samples were excited, respectively, at 405, 488, 561 and 633 nm, with emission bands of 420–446 nm, 495–540 nm, 570–620 nm and 640–680 nm, using PMT detectors for DAPI, TO-PRO-3 and H3S10ph and a hybrid detector for microtubules. All roots were imaged ensuring that no pixel was saturated, with the same laser or diode power, same AOTF, same PMT level, no offset and a line average of 2.

Image analysis

To ensure the representativeness of the data and to buffer the impact of any individual root with an unusually low or high signal range, between 6 to 8 roots for each treatment or genotype were used. We also excluded any roots with a poor signal-to-noise ratio, which may arise if the roots were damaged or had suffered during the immunolocalization protocol. All image processing steps were performed in Fiji (Schindelin *et al.*, 2012). Pipelines were written as ImageJ macros using functions from the BoneJ2 (Domander *et al.*, 2021) and MorphoLibJ (Legland *et al.*, 2016) ImageJ plugins. A manual for the installation and use of the three macros developed in this article is available as Supporting Information Methods S1. The macros are available as Methods S2–S4.

The 'Attenuation Correction' plugin (Biot *et al.*, 2008) and the 'Bleach Correction' tool of ImageJ (Miura, 2020) were tested for the correction of signal attenuation. For the Bleach Correction tool, we used the Simple Ratio Method with a background level set to 15; tests were also performed with background levels set at 0 and 10, with no further improvement. For the Attenuation Correction plugin, we took as the reference slice the first (upper-most) slice containing objects and a radius of 1. Radius from 2 to 5 were also tested with no further improvement. None of these two methods proved to be suitable to correct H3S10ph signal attenuation with Z.

Graphs were generated with ggplot2 and Excel.

Results

Automatic detection of Histone H3 Ser10 objects

3D imaging of H3S10ph signal dynamics during mitosis in Arabidopsis root tip cells Whole-mount immunolocalization of root tips is the method of choice to visualize a high number of dividing cells representative of each mitotic phase, allowing recording a dynamic signal in space and time during mitosis (Belcram *et al.*, 2016; Schaefer *et al.*, 2017). In order to visualize and quantify the H3S10ph signal in dividing cells of Arabidopsis, we performed whole-mount immunolocalization of root tips using an anti-H3S10ph antibody together with an anti-tubulin antibody and DAPI staining, and acquired full 3D stacks of the entire root tip (Fig. 1). In control Col0 Arabidopsis seedlings, the H3S10ph signal is highly specific, with a high signal to noise ratio (Fig. 1d). It shows up very transiently during mitosis, appearing during early mitosis, in cells harboring a mature preprophase band (PPB), and disappearing during anaphase (Fig. 1e–l). Based on both the microtubule and H3S10ph signals, we could define five stages of Histone H3 positive cells: (1) The Early Prophase stage corresponds to cells with a preprophase band (Fig. 1f), (2) the Late Prophase stage comprises cells exhibiting a prospindle (Fig. 1g), (3) the Prometaphase stage corresponds to cells with a mitotic spindle before full chromosome congression (Fig. 1h), (4) the Metaphase stage where the chromosome alignment is complete with a clear metaphase plate (Fig. 1i) and (5) the Anaphase stage when the chromosomes move to opposite ends of the cell (Fig. 1j). The signal then completely vanishes in Telophase (Fig. 1l).

Automatic object segmentation and recognition We next took advantage of the high specificity and low background of the H3S10ph signal in the 3D images to set up an ImageJ pipeline to automatically segment and measure the total H3S10ph signal within each mitotic cell. The challenge here was that H3S10ph signals are morphologically highly variable according to the mitotic stage considered (Fig. 1e–l). In prophase, the signal is a dotted pattern, with each dot corresponding to a condensed chromosome (Fig. 1e,f). In metaphase, signal morphology corresponds

New Phytologist

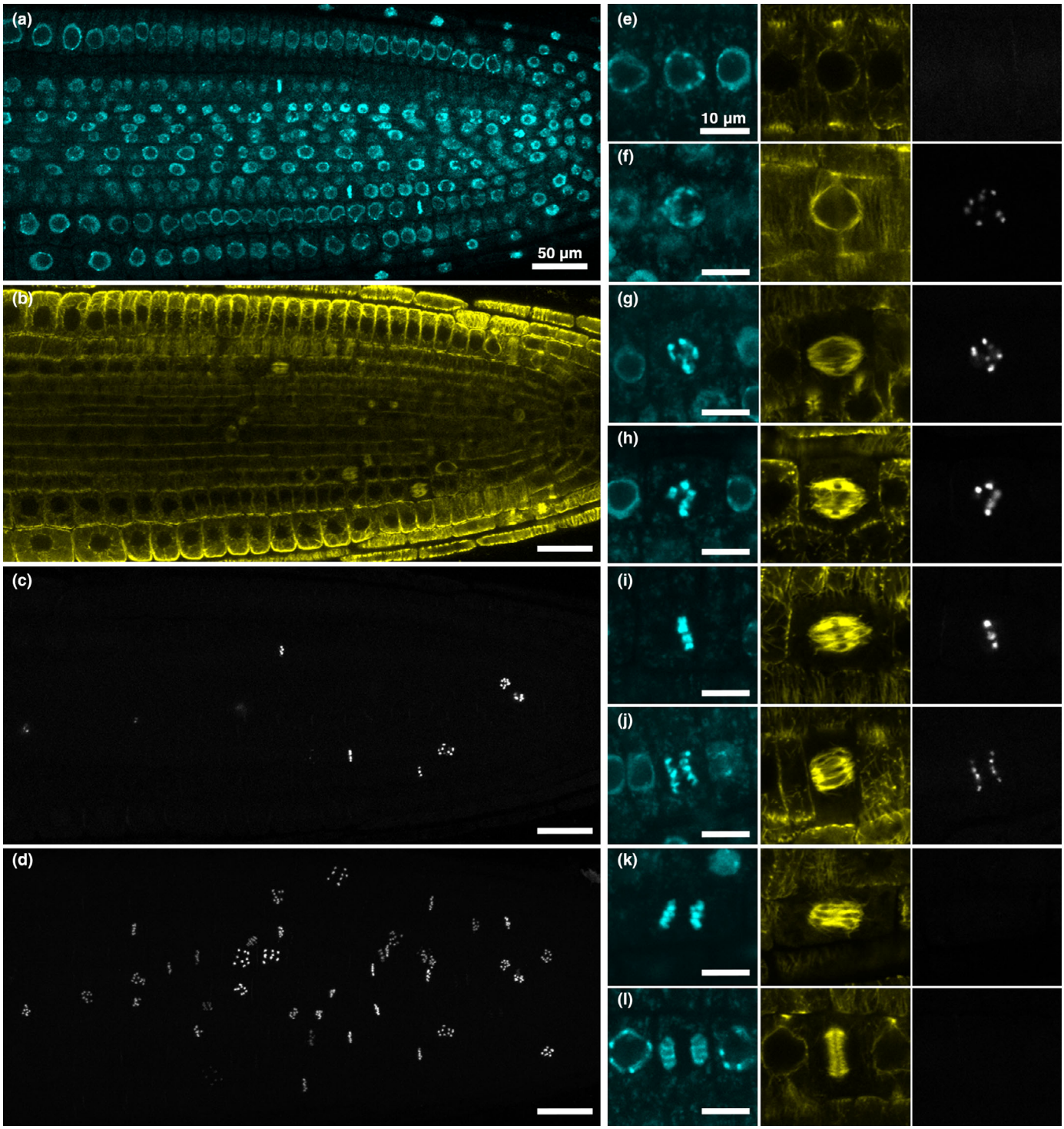

Fig. 1 Dynamic distribution of phosphorylation of histone H3 at serine 10 (H3S10ph) signal in Arabidopsis root tips. (a–c) Longitudinal sections of the root tip, showing the DNA (4′,6-diamidino-2-phénylindole (DAPI) staining in (a)), microtubule organization (anti-tubulin in (b)) and the H3S10ph signal (anti-histone H3 (phospho S10) in (c)). (d) Maximum projection of the H3S10ph signal. (e–l) Close-ups of dividing cells illustrating H3S10ph signal dynamics during mitosis. (e) The H3S10ph signal was never detected in cells with an immature preprophase band (PPB) (large PPB and/or few perinuclear microtubules). (f) The H3S10ph signal appeared at the late PPB stage when perinuclear accumulation of microtubules was prominent. This stage was defined as early prophase in this study. (g) Late prophase corresponded to cells at the prospindle stage. (h) At the prometaphase stage, chromosomes started to congress. (i) Chromosome congression culminated at the metaphase stage with the establishment of a metaphase plate. (j, k) In anaphase, the H3S10ph signal was still visible in early anaphase as sister chromatids moved to the poles (j) then disappeared in late anaphase (k). (l) The H3S10ph signal was never observed during cytokinesis, in cell containing a phragmoplast. Bars: (a–d) 50 µm; (e–l) 10 µm. DAPI staining in blue, microtubules in yellow and H3S10ph signal in gray.

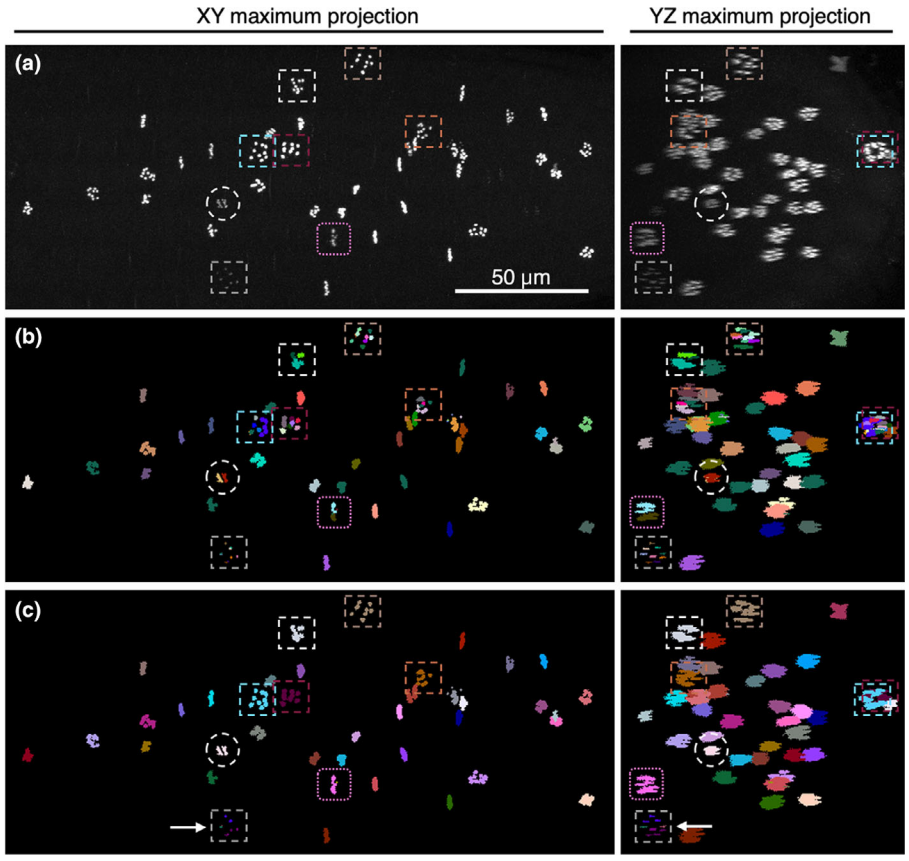

Fig. 2 Automatic objects segmentation and recognition. (a) Maximum intensity projection of the H3S10ph channel from an Arabidopsis root three-dimensional (3D) stack. (b) Maximum projection of the 3D particle map. (c) Maximum projection of the 3D stack after fusion of labels. One the left, XY maximum projections, and on the right, YZ projections of the same 3D stack. Highlighted boxes/circles correspond to merged labels. Here are shown six early prophase nuclei (dotted rectangles), one anaphase nucleus (circle) and one metaphase nucleus (pink rounded square) cells. Note that some chromosomes of a same cell may not be fully fused after this process (here an early prophase object highlighted with a gray rectangle and a white arrow at the bottom of the images). Bar: (a) 50 µm.

to a disk-shaped plate, the metaphase plate (Fig. 1i). In anaphase, the signal corresponds to two disk-shaped objects corresponding to the two sets of genetic material moving toward the poles (Fig. 1j).

Our pipeline takes as input the H3S10ph 3D stack (12-bit images, Fig. 2a), which is first binarized using an (adjustable) gray value threshold (usually *c.* 150). Particles (sets of connected voxels) are then labeled individually and their volumes computed, thus enabling the selection of only those particles with a volume above the smallest *bona fide* H3S10ph signal (*c.* 0.4 μm^3 here). Since chromosomes from the same cell are often segmented as independent particles, especially in prophase or anaphase, we need to group particles from the same cell into a single label. For this, the image of selected particles is transformed into a binary image that is dilated using a 3D spherical structuring element with a radius of 3–4 voxels (i.e. smaller than a typical nucleus size). The dilation radius is adjusted in order to avoid fusion of chromosomes from adjacent cells (Fig. S1; Methods S1). This operation results in aggregates connecting all particles within a single cell, and these aggregates are then labeled individually, with each label encompassing the signal from a single cell. The resulting label image is then masked by the binary image of particles created earlier, producing a final image of labeled particles in which distinct particles from the same cell are assigned the same label (Fig. 2c). This final label image is used to obtain the total fluorescence signal in each cell from the original H3S10ph channel. The total fluorescence signal is calculated for each label by multiplying its mean gray value with its volume in voxels and is hereafter designed as 'integrated density'.

More than 95% of nuclei are correctly unified with this method designed to assign a single label to particles belonging to the same cell. For instance, in Dataset S1 of Fig. 6(a) where 23 roots were analyzed, a total of 967 nuclei were identified, in which only 32 imperfectly fused nuclei remained to be unified in the final dataset by human curation (30 nuclei split into two labels and two into three parts). In these rare instances, where chromosomes from the same cell were not completely unified, that is, represented by two or more labels (see Figs 2c, S1c), their values were added manually in the final results table.

Correction of signal attenuation with depth

H3S10ph signal decreases with *z* depth We first applied the above protocol on Col0 control roots. Plotting the integrated density of H3S10ph signals against *z* depth (expressed as slice number) for the eight Col0 stacks (*c.* 260 mitotic cells) revealed a strong signal attenuation (Figs 3a,b, S2), that is, signal intensity decreasing with *z* depth in the stacks, with the average signal dropping as much as 2–4-fold from the top to the bottom of the stack (*c.* 100 µm) (Fig. 3a,b). Obviously, such strong attenuation was precluding signal intensity measurements in 3D. In an attempt to circumvent this problem, we applied two independent correction algorithms to preprocess our images. A classical tool available as an ImageJ plugin, the 'Attenuation Correction'

New Phytologist

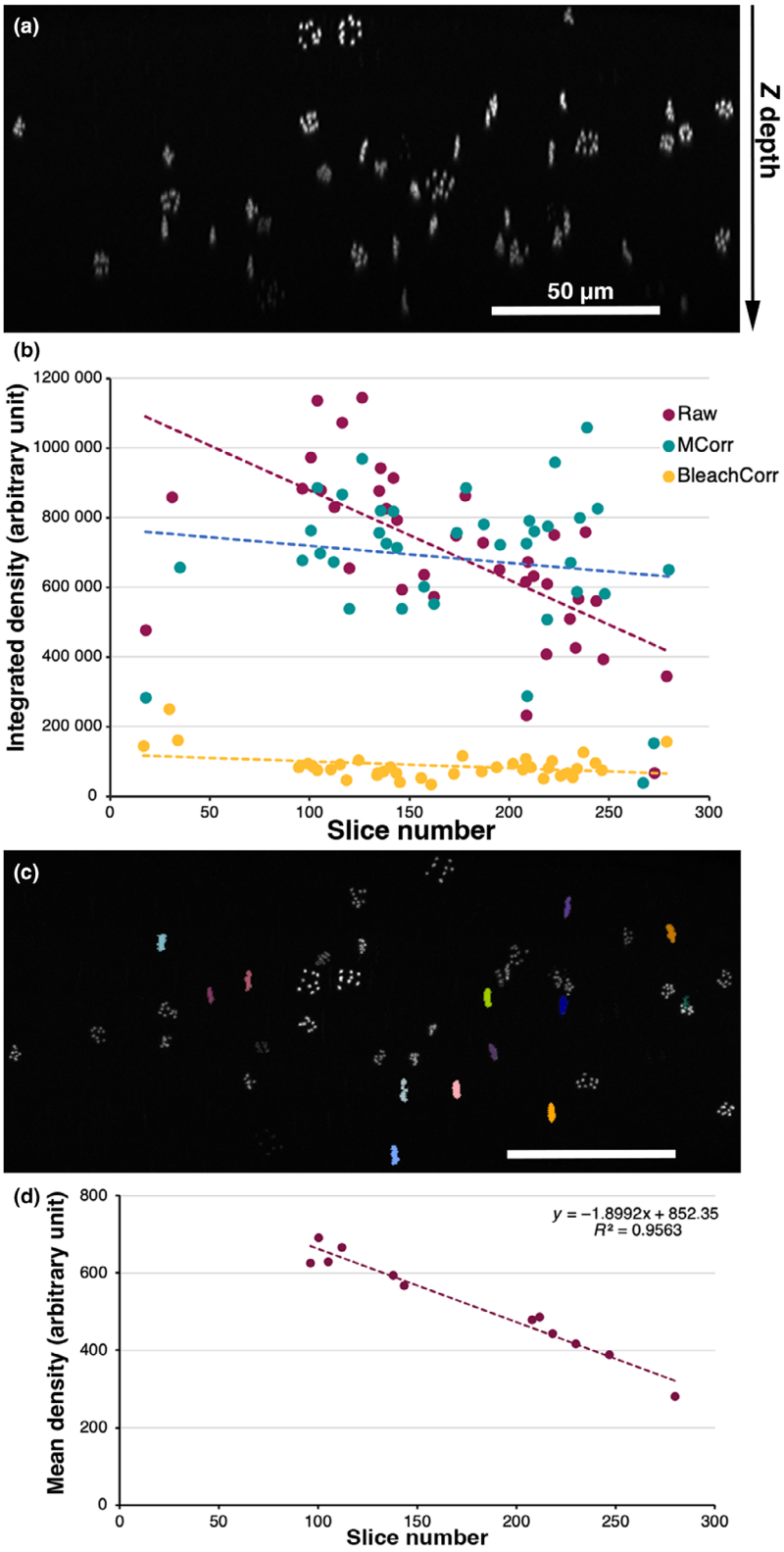

Fig. 3 Correction of the H3S10ph signal attenuation. (a) Maximum projection of an Arabidopsis three-dimensional (3D) stack in the XZ plane, showing signal attenuation with *z* depth. The *z*-axis is indicated on the right. (b) Graph plotting the integrated density of each H3S10ph-positive cell against *z* depth of the same 3D stack. In purple, the raw integrated density, in blue the integrated density of H3S10ph objects corrected using the correction based on the metaphase objects (Metaphase Correction 'MCorr') and in yellow, the integrated density of H3S10ph objects corrected using the Bleach Correction tool of ImageJ (BleachCorr). (c) Maximum projection of the root stack (in the XY plane), where the filtered metaphase objects are colored. (d) Graph plotting the mean density of metaphase objects shown in (c) against the slice number. Bars: (a, c) 50 µm. Regression lines in (b) and (d) are dotted. The R^2 coefficient and the equation are indicated at the top right of the graph in (d).

plugin (Biot *et al.*, 2008), did not seem adapted to the sparse discrete objects and low background obtained after immunolocalization with the H3S10ph antibody. Signal correction was erratic along slices of the stack, impairing signal integrity and thereby compromising particle detection and segmentation (Fig. S3). We also evaluated the 'Bleach Correction' tool available in ImageJ, by comparing the integrated density of all objects before and after correction, and plotting their values against *z* depth. This tool

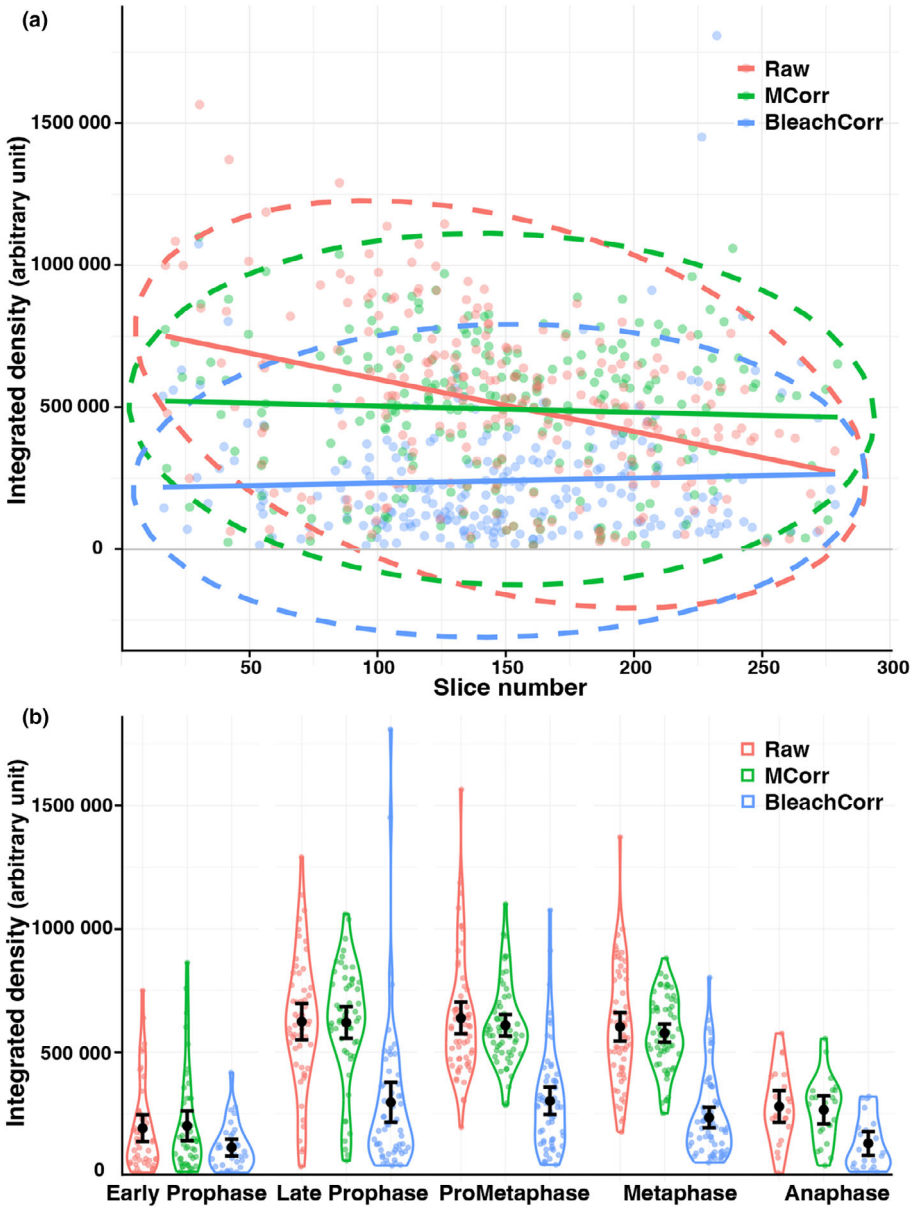

Fig. 4 Comparison of the Bleach Correction and the Metaphase Correction (MCorr) methods. (a) Graph plotting the integrated density of all H3S10ph objects against slice number for the eight Col0 Arabidopsis roots analyzed. The regression lines and ellipse are superimposed on the graph. (b) Graph showing the dynamics of histone phosphorylation during mitosis in raw data and after correction using the MCorr and the Bleach correction tools. The means and the 95% confidence intervals are superimposed on the violin plots, which depict the data distributions. The CI95 was reduced when the objects' integrated densities were corrected using the MCorr (up to 36.8% for the metaphase stage and 33.2% for the prometaphase stage compared to raw data). In red, the raw values (Raw); in green, values corrected using the correction based on the metaphase objects (MCorr) and in blue, values corrected using the Bleach Correction tool of Fiji (BleachCorr).

did indeed correct signal attenuation in some roots (Fig. 3b), but the correction was highly variable, with some roots being corrected and others not (Fig. S2). Moreover, the 'Bleach Correction' tool crushed signal dynamics (Figs 4, S2), preventing its use for signal quantification.

We next explored the possibility of normalizing the H3S10ph signal to the 4',6-diamidino-2-phénylindole (DAPI) one. For DAPI (or another nuclear signal such as TO-PRO-3) to serve as an internal control, its attenuation with depth should mirror that of the H3S10ph signal, and its intensity should remain constant throughout the cell cycle. However, neither of these two conditions was fulfilled (Fig. S4).

Attenuation Correction on metaphase objects We finally explored if we could directly and quantitatively assess the attenuation of discrete H3S10ph objects, in order to correct the images accordingly. Since the phosphorylation signal inherently varies from one mitotic stage to the next, increasing in prophase and dropping in anaphase, we decided to assess signal attenuation on a homogeneous category of objects. The metaphase stage is very short in Arabidopsis root meristematic cells (3–5 min), and the H3S10ph signal intensity is expected to show little variation from one metaphase object to another. Therefore, we chose metaphase objects to assess z attenuation.

We took advantage of the label/cell image obtained previously that can then be used not only to measure H3S10ph signal intensity per mitotic cell, but also to filter labels based on their size and shape. This revealed that metaphase objects could be automatically detected and isolated from all other H3S10ph objects based on their specific geometry (Fig. S5). Indeed, the flatness

indices of metaphase labels were statistically different from all other labels. In addition, their sphericity was comparable to that of prometaphase objects, but differed from all other labels (Fig. S5). Using these two criteria, we automatically extracted metaphase objects with a high degree of confidence, and 6–12 metaphase objects were retrieved per 3D stack (Figs 3c,d, S6). Plotting the mean intensity of metaphase objects over slice number showed that signal loss was a linear function of slice number. We thus applied a linear regression, resulting in good R^2 coefficients (Figs 3d, S6). The regression parameters were then used to calculate correction factors for all slices.

The corrected stacks were then subjected to the same procedure as described above for signal quantification (thresholding, segmentation, etc.) and results were compared to uncorrected stacks.

Benefits of correcting signal attenuation To evaluate the benefit of the correction based on metaphase objects (hereafter referred to as the 'Metaphase Correction', MCorr in short), we measured the integrated density of all objects before and after MCorr in the eight Col0 roots and plotted the integrated density values against root depth expressed as slice number (Figs 4a, S2). This indeed showed that the integrated density of the signal was well corrected using this method. We then plotted the ratio between the mean, volume and integrated density before and after MCorr (Fig. S7). It appeared that, as expected, the major effect of the correction was on the volume of the objects, their mean signal value being only marginally modified (Fig. S7). Correction indeed mostly played on particle segmentation by thresholding, increasing or decreasing the number of voxels of a given object depending on its z position and played only to a lesser extent on its average grey value. These graphs also revealed that some rare objects were more corrected in volume than others, mostly in the lower part of the stack. On closer analysis, they were all annotated as early prophase objects (Fig. S7). Such early prophase cells showed a weak and very fragmented signal (corresponding to the 10 Arabidopsis chromosomes), by nature particularly sensitive to volume changes induced by the correction (as mentioned in the previous section).

Increased reliability brought about by MCorr resulted in reduced 95% confidence intervals (Fig. 4b; Dataset S1), by up to 37% for the metaphase stage and 33% for the prometaphase stage, compared to measures obtained from uncorrected images. In addition, as detailed below, the MCorr procedure was very efficient in compensating for uneven distribution of objects in z that can happen by chance in some samples.

A set of ImageJ Macros to measure signal intensity

In order to automatize H3S10ph signals measurement, we developed three ImageJ macros. These three macros, along with a full tutorial, are available as Methods S1–S4.

Correction A first macro ('HisCorrect', Methods S2) was designed to automatically detect metaphase objects, calculate the regression curve and correct the z-stack images accordingly. The macro uses the BoneJ segmentation and MorphoLibJ morphological selection tools (size, flatness and sphericity) to detect specific objects like, in our case, metaphase plates. The threshold value, minimum object volume and dilation radius can be adjusted by the user as well as the size, flatness and sphericity thresholds. However, morphological selection is not always 100% correct, and some nonmetaphase objects may sometimes pass the filters (Fig. S8). To remove these misclassified objects, we introduced the ability in the HisCorrect macro to visually check the object filtering and remove any nonmetaphase objects from the regression dataset, resulting in a better regression fit (Fig. S8). All roots with an R^2 coefficient < 0.4 were removed from the analysis. The macro then applies a correction coefficient based on the predicted values of the regression, taking the center slice as reference. As the slope is negative, the signal of top slices is lowered, whereas it is increased in the bottom ones. The output of the macro includes the corrected z-stack image, and optionally the regression plot, the original BoneJ label image, and the object map before filtering.

Optionally, the macro can also calculate a regression on all objects, without prior filtering. Indeed, some treatments or genotypes may greatly affect the number of dividing cells present in the root tip. In such images there are not enough metaphase objects to calculate a proper regression. In this case, the user may inactivate the shape-based selection to use all the H3S10ph objects for calculating the correction (Fig. 6c).

Measurement The second macro ('HisMeasure') was designed to measure the integrated density of H3S10ph objects from the original or corrected images. The macro operates on the same principle as the HisCorrect macro. If needed one can also adjust the threshold value, the minimum volume of objects and the dilation radius as well as the size, flatness and sphericity ranges to remove unwanted background labels. The signal parameters (mean, SD, max, min, median, integrated density, etc.) are returned as a table, together with a number of parameters on object position, size and shape. If requested, as before, all 3D object maps and their projections can be saved.

Annotation The third macro ('HisAnnot') allows to quickly annotate each object detected, for example, in our case for its mitotic stage. The macro highlights each label/H3S10ph object on the root stack image one by one and allows a category to be selected and assigned. In our case, the category is the mitotic stage (early prophase, late prophase, prometaphase, metaphase, anaphase), but that can be adjusted if needed.

Detection of histone phosphorylation inhibition after the Aurora inhibitor hesperadin treatment

To evaluate the ability of our pipeline to quantify H3S10ph signals and to detect differences under conditions known to affect this process, we treated Arabidopsis roots with the Aurora kinase inhibitor hesperadin. Two hesperadin treatments were applied for 24 h on 3-d-old seedlings, one at 1 μM and the other at 5 μM. We counted cells harboring mitotic microtubular

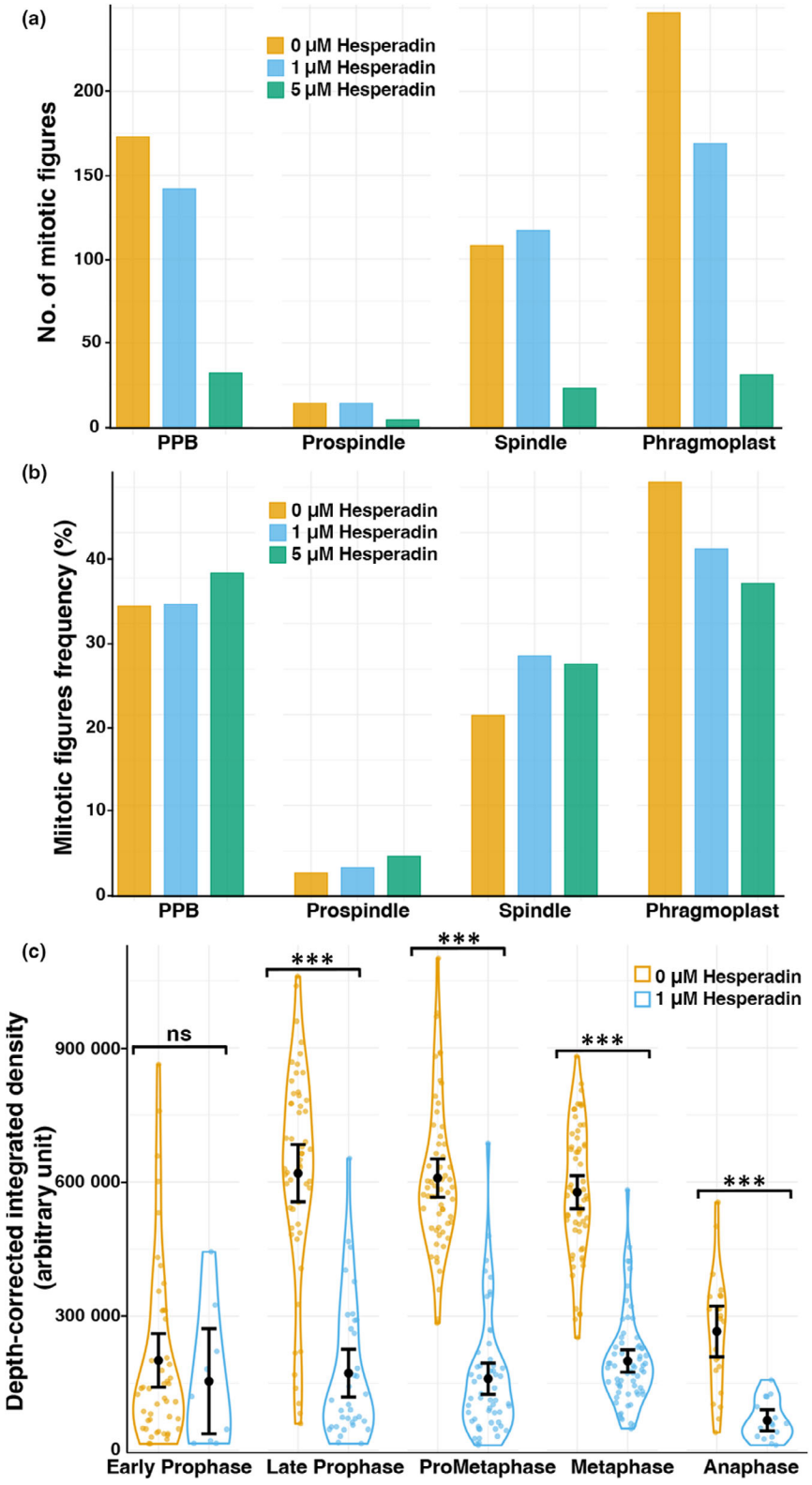

Fig. 5 Hesperadin treatment affects phosphorylation of histone H3 at serine 10 (H3S10ph). (a, b) Hesperadin treatment reduced dividing cells frequency. Mitotic microtubule arrays were counted in five Arabidopsis roots for the control and for each treatment (a). The frequency (%) is illustrated in the graph in (b). (c) Graph showing the strong reduction in H3S10ph signals after treatment with 1 µM hesperadin (eight roots analyzed for each condition). In yellow, the control; in blue, the 1 µM Hesperadin treatment; in green, the 5 µM hesperadin treatment. The means and the 95% confidence intervals are superimposed on the violin plots, which depict the data distributions. Nonparametric tests were used for comparing samples (Mann–Whitney). The stars above the graph indicate whether the difference between the means is statistically significant or not (***, $P < 0.05$; ns, nonsignificant).

structures (PPB, spindles and phragmoplasts) and showed that the 5 µM treatment dramatically affected the number of dividing cells (Fig. 5a). The relative frequency of mitotic phases was, however, mostly unaffected (Fig. 5b). We then set out to measure the effect of hesperadin on H3S10ph levels. In untreated root tips, the signal started to appear during prophase in cells harboring a mature PPB, was already at its maximum in late prophase, stayed high in prometaphase and metaphase and decreased and

New Phytologist

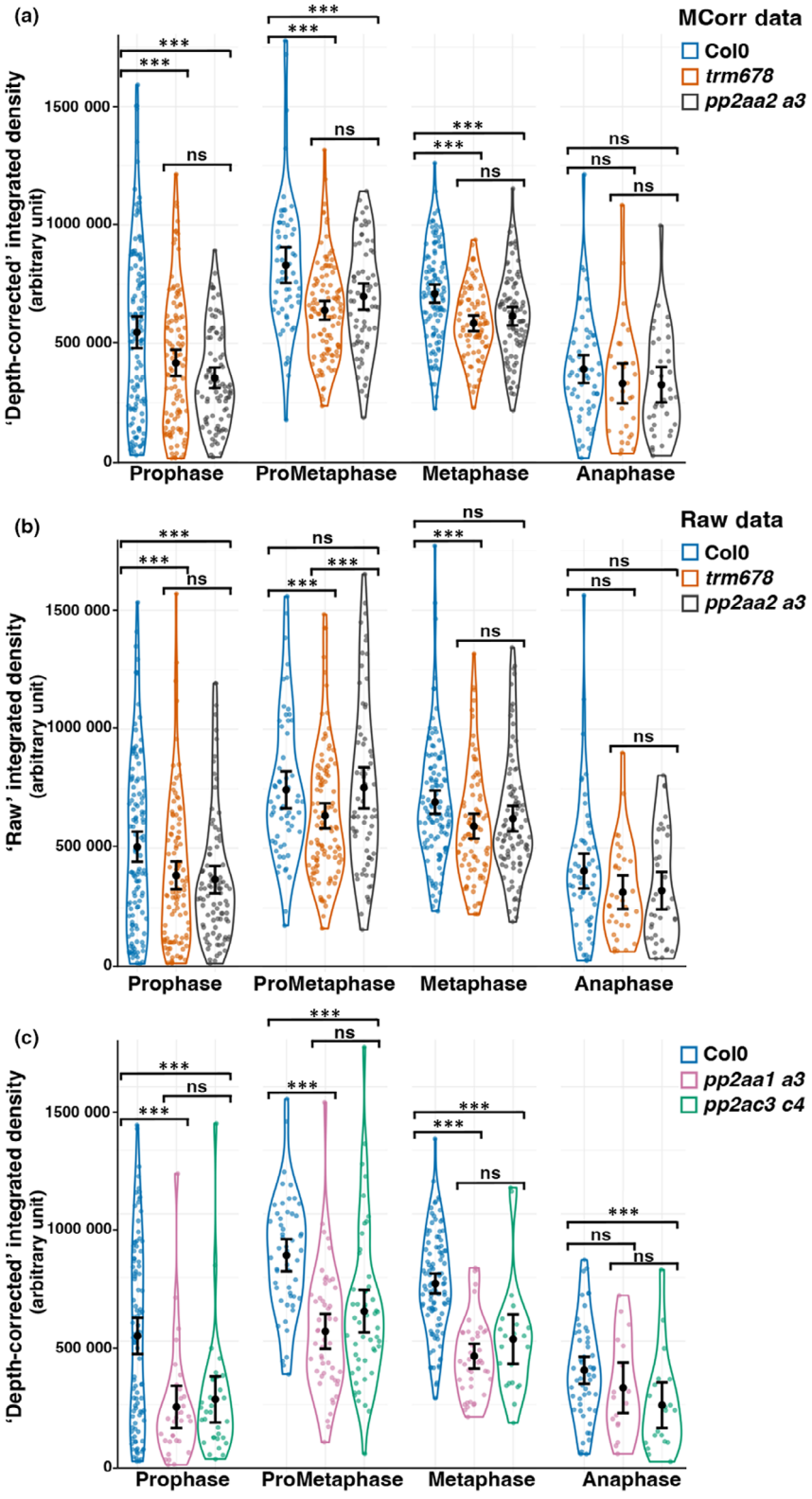

Fig. 6 *pp2a* mutations affect phosphorylation of histone H3 at serine 10 (H3S10ph). (a, b) Measurement of integrated density of the H3S10ph signal in the Arabidopsis wild-type (Col0), the *trm6 trm7 trm8* triple and the *pp2aa2 pp2aa3* double mutants. In (a), the analysis was performed on corrected data, whereas (b) represents raw data analysis. Note that in prometaphase, the correction makes previously insignificant data statistically significant (see also Supporting Information Fig. S10). (c) Comparison of phosphorylation signals between the control, *pp2ac3 pp2ac4* and *pp2aa1 pp2aa3* double mutants. Signal correction was done using a regression performed on all objects rather than on metaphase objects, which were too rare to draw a robust regression line. *pp2ac3 pp2ac4* and *pp2aa1 pp2aa3* double mutants are indeed strongly affected in their development and both mutations strongly reduced the number of dividing cells. Nonparametric tests were used for comparing samples (Mann–Whitney). The stars above the graph indicate whether the difference between the means is statistically significant or not (***, $P < 0.05$; ns, nonsignificant). Adjusted *p*-values are shown in Supporting Information Fig. S9. Number of analyzed roots = 8 (Col0 and *pp2aa2 pp2aa3*), 7 (*trm678* and *pp2aa1 pp2aa3*) and 6 (*pp2ac3 pp2ac4*). The means and the 95% confidence intervals are superimposed on the violin plots, which depict the data distributions.

disappeared during anaphase (Fig. 5c; Dataset S1). The 5 μM hesperadin treatment drastically reduced the number of H3S10ph-positive cells, from 0 to a maximum of 4 cells per root, preventing any quantification. Treatment with 1 μM hesperadin severely reduced H3S10ph levels from late prophase to anaphase, with a decrease of up to 75% compared to untreated seedlings. However, it had no significant effect on the level of H3S10ph in early prophase, suggesting that Aurora is not the only kinase involved in H3S10ph at this stage or that hesperadin is not active at this stage.

Our pipeline thus enables us to precisely measure H3Ser10ph levels and for the first time to study with great accuracy the dynamics of this signal during mitosis in plants. Using a microtubule antibody along with the H3S10ph antibody, all mitotic phases were readily resolved in our analysis. If needed, the time resolution can even be increased using supplemental markers of mitotic progression.

Role of PP2A enzymes in Histone H3 phosphorylation on Ser10

To determine whether PP2A phosphatase enzymes could play a role in H3S10ph status, we set out to quantify the H3S10ph signal in several mutants impaired in PP2A activity. PP2A holoenzymes are ubiquitous phosphatases involved in a variety of cellular processes (Janssens & Goris, 2001). PP2A phosphatases are trimeric enzymes composed of a catalytic subunit (PP2A-C), a regulatory subunit (PP2A-B) and a structural subunit (PP2A-A) (Shi, 2009). In Arabidopsis, PP2A-A subunits are encoded by three genes, the PP2A-A1 subunit playing a major role compared to PP2A-A2 and PP2A-A3 isoforms. Indeed, *pp2aa2 pp2aa3* (hereafter *a2/a3*) double mutant plants have no developmental phenotype, whereas *pp2aa1* single mutant, *pp2aa1 pp2aa3* (*a1/a3*) and even more *pp2aa1 pp2aa2* (*a1/a2*) double mutant plants have strong developmental defects (Zhou *et al.*, 2004). PP2A-C subunits are encoded by five genes divided into subfamily I (PP2A-C1, -C2 and -C5) and subfamily II (PP2A-C3 and -C4). Hypomorphic *pp2ac3 pp2ac4* (hereafter *c3/c4*) double mutants are dwarf plants with small and thick leaves, thick flowering stems and impaired root growth (Spinner *et al.*, 2013). We thus assessed H3S10ph dynamics in *a2/a3*, *a1/a3* and *c3/c4* backgrounds. In addition, we also studied histone phosphorylation in a *TON1 Recruiting Motif (trm)* mutant. TRM proteins are part of the TTP complex (for TON1-TRM-PP2A), a complex composed of TON1, a TRM isoform and a PP2A enzyme with FASS as the regulatory subunit (Spinner *et al.*, 2013). The TTP complex is involved in the spatial organization of cortical microtubules, and TRM6-TRM7-TRM8 proteins have been shown to play an important role in PPB assembly. In contrast to *fass* or *ton1* mutants that display extreme and severe dwarfism, the *trm678* triple mutation results in a mild phenotype that is easily amenable to whole-mount immunolocalization (Schaefer *et al.*, 2017).

We started by measuring histone H3S10ph in mildly affected genotypes like the *a2/a3* and *trm678* mutants. Eight (Col0 and *a2/a3*) or seven (*trm678*) roots were analyzed for H3 phosphorylation. Since *trm678* mutant cells lack the PPB used to define early prophase, we classified the histone signal into only four classes; that is, prophase, prometaphase, metaphase and anaphase. To evaluate the benefit of our attenuation correction method, we also analyzed the same data with and without correction.

The analysis performed on corrected data showed that the H3S10ph signal is significantly reduced in both mutants for all stages except anaphase (Figs 6a, S9; Dataset S1), showing that PP2A activity is necessary to activate Histone H3 phosphorylation. The involvement of the TTP complex is rather unexpected in this context but may point to a link between interphasic and mitotic arrays of microtubules and control of spindle formation by the PPB (Bouchez *et al.*, 2024).

As shown previously, comparison of data before and after correction confirmed that the MCorr treatment significantly reduced the confidence intervals (Figs 6, S9). Interestingly, it also illustrated that this procedure can correct for uneven localization of objects within the biological samples and original stack images. Here, analysis of raw data did not reveal any difference between the wild-type and the *a2/a3* mutant at the prometaphase stage (Figs 6b, S9), whereas corrected data unambiguously did (Figs 6a, S9). Analysis of the distribution of prometaphase cells within the 3D images revealed that in this particular subset, prometaphase cells were preferentially located toward the lower half of the stacks in the wild-type roots, whereas *a2/a3* prometaphase cells were biased toward the top half of the 3D images (Fig. S10). Thus, in addition to globally decreasing confidence intervals, the method allows for handling uneven distribution of objects within 3D stacks as well. Our correction method is thus particularly suited to unravel small-amplitude genetic or experimental effects that would be masked by depth attenuation.

We finally quantified H3S10ph dynamics in severely impaired mutants, that is, *a1/a3* (7 roots) and *c3/c4* (6 roots) double mutants, both impaired in PPB formation as *trm678* (Spinner *et al.*, 2013) (Figs 6c, S9; Dataset S1). In these genotypes, root morphogenesis was severely affected, and the number of dividing cells, including cells in metaphase, was strongly reduced, making it difficult to use a correction solely based on metaphase objects. We therefore used all H3S10ph objects to calculate the regression. Again, this showed that the level of H3S10ph is strongly reduced in the *a1/a3* and *c3/c4* double mutants, confirming that PP2A activity is involved in the control of H3S10ph by Aurora kinases. The control Col0 samples common to both comparisons displayed very similar values after correction (compare Col0 in Fig. 6a to Col0 in Fig. 6c), indicating that although expectedly less precise, correcting on all objects may also be an interesting alternative when metaphase cells are not sufficient to use the MCorr strategy.

Discussion

PTM of histones during the cell cycle is a major process controlling many aspects of cellular life, including division. Among them, mitotic H3S10ph is an archetypal example that has been intensively studied in animal cells. Here we developed a new tool based on image analysis to measure the dynamics of H3S10ph levels during the cell cycle in plant cells and set up an original object-based attenuation correction method to compensate for signal attenuation in z in 3D confocal stacks.

One major advantage of our image-based quantification method is the ability to resolve analyses according to specific cell cycle phases. This approach eliminates the need for chemical perturbations typically used to synchronize cells before Western blot analysis, a standard protocol for measuring histone phosphorylation during the cell cycle (i.e. Wang *et al.*, 2023). In addition, while synchronization methods are available for Arabidopsis root

cells (Cools *et al.*, 2010) or cell culture (Menges & Murray, 2002), they generally achieve only limited synchronization efficiency. As a result, these methods are not well suited for detailed analysis of dynamic signals such as H3S10ph. By contrast, our method enables precise, phase-specific quantification without introducing artefacts associated with synchronization treatments.

We used confocal imaging to acquire and analyze the H3S10ph signal in three dimensions. By acquiring 3D images, we were able to integrate the entire H3S10ph signal for each cell, which significantly improved measurement accuracy compared to classical 2D analyses (Garda *et al.*, 2018; Ujvárosi *et al.*, 2019). We developed a pipeline that enables semiautomatic extraction, quantification and annotation of H3S10ph signals in full 3D. This tool runs with Fiji–ImageJ, an open-source Java image processing program, thus freely accessible to the community (Schindelin *et al.*, 2012).

A key challenge in quantifying signals within 3D confocal stacks is the pronounced attenuation of signal intensity with depth. A classical solution for signal quantification is the use of ratiometric approaches, where the signal of interest is normalized to a reference signal that is constant across the condition tested. Ratiometric methods will efficiently compensate for *z*-attenuation but, as attractive as they may look, they will often prove difficult if not impossible in practice, due to the difficulty of designing a reliable reference marker for normalization (see Fig. S4). Alternatively, background-based attenuation measurements classically used are generic in nature and can be very efficient in correcting for *z* attenuation (e.g. Biot *et al.*, 2008). However, these methods typically rely on specific assumptions, such as an expected depth-independent background (Biot *et al.*, 2008) or constant average intensity per slice (Miura, 2020). In cases, where these assumptions do not hold, such as here with a low and constant background and a low and varying number of discrete objects, such methods can produce erratic results (Fig. S3). The method and algorithms developed in this work provide a new and original solution to this classical problem.

The MCorr method is based on a detailed analysis of the signal in individual images, selection of the most constant objects, and calculation of the attenuation slope for correction. The only requirement here is that the biological objects of interest (i.e. to be measured) could be extracted from the image by segmentation. MCorr proved to be effective in decreasing value dispersion of objects and in reducing confidence intervals, especially for late prophase, prometaphase and metaphase signals (Figs 4, 6). In addition, MCorr was also very efficient in correcting for uneven distribution of objects within the depth of 3D stacks (Fig. 6). Consequently, this tool allowed detection of small effects between biological treatments/genotypes with strongly increased statistical power. Although initially developed based on an estimation of signal decrease of metaphase objects over *z* depth, MCorr can also be used to correct images based on the signal decrease of all objects, as exemplified here for the study of mutations reducing cell division activity (Fig. 6). It is also worth noting that the MCorr method could be applied to any other PTM histone signal and, more generally, any discrete 3D signal amenable to segmentation, provided a few adaptations and adjustment of settings.

To accurately monitor mitotic stages, we used microtubule labelling, which allowed us to track H3S10ph signal dynamics during mitosis with exceptional precision, achieved for the first time in plants. We have shown that the H3S10ph signal appears during early prophase, is highest in late prophase in the wild-type, then remains at the same high level until metaphase, declines rapidly during anaphase and is undetectable at the end of anaphase. We did not observe any interphasic H3S10ph signal in interphase nuclei, as has been observed in animal cells, or in differentiated tobacco mesophyll cells (although at very low levels) (Hendzel *et al.*, 1997; McManus & Hendzel, 2006; Granot *et al.*, 2009; Sawicka & Seiser, 2012). As expected for an inhibitor of Aurora, the kinase responsible for H3S10ph (Kurihara *et al.*, 2008; Demidov *et al.*, 2009), hesperadin treatment drastically perturbed H3S10ph dynamics. One micromolar hesperadin treatment of Arabidopsis seedlings reduced H3S10ph level by 75% in the root tip (Fig. 5). However, it did not affect H3S10ph levels in early prophase, which could reveal a yet-to-be-discovered kinase responsible for H3S10ph at this early stage of division. Hesperadin treatment had also a high impact on division itself. As already noted (Kurihara *et al.*, 2006), hesperadin affects cell cycle progression and the metaphase/anaphase transition (Fig. 5a). At 5 μM, it nearly abolished cell division in Arabidopsis roots. Tobacco BY2 and Arabidopsis cultured cells appeared less sensitive to hesperadin than Arabidopsis roots, since 5 μM hesperadin treatment in these culture cells did not seem to affect cell cycle progression (Kurihara *et al.*, 2006; Demidov *et al.*, 2009).

Measurement of H3S10ph signals in *pp2a* mutant revealed that PP2A enzymes may be indirectly involved in regulating H3S10ph levels, since impairing PP2A phosphatase activity reduced Histone H3 phosphorylation. This is reminiscent of the observation that PP2A activity promotes Aurora inactivation in mammalian cells (Carmena *et al.*, 2009), both directly by dephosphorylating the kinase (Eyers *et al.*, 2003) or indirectly by stabilizing PTTG1, an inhibitor of Aurora (Tong *et al.*, 2008). This shows that this new approach, which enables the detection of subtle yet robust differences between genotypes or treatment, opens exciting new avenues for exploring histones phospho-regulation pathways in plants using the wealth of genetic resources available in Arabidopsis.

Acknowledgements

This work was supported by the EMBO Scientific Exchange Grants to AK and by ANR-20-CE13-0026-02 to DB. It has benefited from the support of IJPB's Plant Observatory platform PO-Cyto and of Saclay Plant Sciences-SPS (ANR-17-EUR-0007).

Competing interests

None declared.

Author contributions

AK, DB and MP designed the research; AK and MP performed the experiments; AK, MP, PA and DB contributed new analytical tools; DB performed the statistical analysis; AK, MU, CM, PA, DB and MP analyzed and discussed the data; DB and MP wrote the article and AK, MU, CM, PA, DB and MP revised and approved the article.

ORCID

Philippe Andrey https://orcid.org/0000-0001-5932-6863
David Bouchez https://orcid.org/0000-0003-3545-4339
Adrienn Kelemen https://orcid.org/0000-0001-7425-7296
Csaba Máthé https://orcid.org/0000-0002-9322-7647
Martine Pastuglia https://orcid.org/0000-0002-5439-7491
Magalie Uyttewaal https://orcid.org/0000-0003-2881-6637

Data availability

Raw confocal images used for implementing and testing our pipeline are available at doi: 10.57745/MKLL9I.

References

Belcram K, Palauqui J-C, Pastuglia M. 2016. Studying cell division plane positioning in early-stage embryos. In: Caillaud M-C, ed. *Methods in molecular biology: plant cell division*. New York, NY, USA: Springer, 183–195.

Beyer D, Tándor I, Kónya Z, Bátori R, Roszik J, Vereb G, Erdődi F, Vasas G, Hamvas M, Jambrovics K *et al.* 2012. Microcystin-LR, a protein phosphatase inhibitor, induces alterations in mitotic chromatin and microtubule organization leading to the formation of micronuclei in *Vicia faba*. *Annals of Botany* **110**: 797–808.

Biot E, Crowell E, Hofte H, Maurin Y, Vernhettes S, Andrey P. 2008. A new filter for spot extraction in n-dimensional biological imaging. In: *2008 5th IEEE International Symposium on Biomedical Imaging: From Nano to Macro*. Paris, France: IEEE, 975–978.

Bouchez D, Uyttewaal M, Pastuglia M. 2024. Spatiotemporal regulation of plant cell division. *Current Opinion in Plant Biology* **79**: 102530.

Carmena M, Ruchaud S, Earnshaw WC. 2009. Making the Auroras glow: regulation of Aurora A and B kinase function by interacting proteins. *Current Opinion in Cell Biology* **21**: 796–805.

Cools T, Iantcheva A, Maes S, Van Den Daele H, De Veylder L. 2010. A replication stress-induced synchronization method for *Arabidopsis thaliana* root meristems: root cell-cycle synchronization method. *The Plant Journal* **64**: 705–714.

Demidov D, Hesse S, Tewes A, Rutten T, Fuchs J, Ashtiyani R, Lein S, Fischer A, Reuter G, Houben A. 2009. Aurora1 phosphorylation activity on histone H3 and its cross-talk with other post-translational histone modifications in Arabidopsis. *The Plant Journal* **59**: 221–230.

Demidov D, Van Damme D, Geelen D, Blattner FR, Houben A. 2005. Identification and dynamics of two classes of aurora-like kinases in Arabidopsis and other plants. *Plant Cell* **17**: 836–848.

Domander R, Felder AA, Doube M. 2021. BoneJ2 – refactoring established research software. *Wellcome Open Research* **6**: 12589.

Eyers PA, Erikson E, Chen LG, Malle JL. 2003. A novel mechanism for activation of the protein kinase Aurora A. *Current Biology* **13**: 691–697.

Garda T, Kónya Z, Freytag C, Erdődi F, Gonda S, Vasas G, Szücs B, Hamvas M, Kiss-Szikszai A, Vámosi G *et al.* 2018. Allyl-isothiocyanate and microcystin-LR reveal the protein phosphatase mediated regulation of metaphase-anaphase transition in *Vicia faba*. *Frontiers in Plant Science* **9**: 1823.

Gernand D, Demidov D, Houben A. 2003. The temporal and spatial pattern of histone H3 phosphorylation at serine 28 and serine 10 is similar in plants but differs between mono- and polycentric chromosomes. *Cytogenetic and Genome Research* **101**: 172–176.

Gil RS, Vagnarelli P. 2019. Protein phosphatases in chromatin structure and function. *Biochimica et Biophysica Acta, Molecular Cell Research* **1866**: 90–101.

Granot G, Sikron-Persi N, Li Y, Grafi G. 2009. Phosphorylated H3S10 occurs in distinct regions of the nucleolus in differentiated leaf cells. *Biochimica et Biophysica Acta (BBA) – Gene Regulatory Mechanisms* **1789**: 220–224.

Hendzel MJ, Wei Y, Mancini MA, Van Hooser A, Ranalli T, Brinkley BR, Bazett-Jones DP, Allis CD. 1997. Mitosis-specific phosphorylation of histone H3 initiates primarily within pericentromeric heterochromatin during G2 and spreads in an ordered fashion coincident with mitotic chromosome condensation. *Chromosoma* **106**: 348–360.

Houben A, Demidov D, Caperta AD, Karimi R, Agueci F, Vlasenko L. 2007. Phosphorylation of histone H3 in plants—a dynamic affair. *Biochimica et Biophysica Acta (BBA) – Gene Structure and Expression* **1769**: 308–315.

Houben A, Wako T, Furushima-Shimogawara R, Presting G, Künzel G, Schubert I, Fukui K. 1999. The cell cycle dependent phosphorylation of histone H3 is correlated with the condensation of plant mitotic chromosomes. *The Plant Journal* **18**: 675–679.

Hsu J-Y, Sun Z-W, Li X, Reuben M, Tatchell K, Bishop DK, Grushcow JM, Brame CJ, Caldwell JA, Hunt DF *et al.* 2000. Mitotic phosphorylation of histone H3 is governed by Ipl1/aurora kinase and Glc7/PP1 phosphatase in budding yeast and nematodes. *Cell* **102**: 279–291.

Janssens V, Goris J. 2001. Protein phosphatase 2A: a highly regulated family of serine/threonine phosphatases implicated in cell growth and signalling. *Biochemical Journal* **353**: 417–439.

Kaszás É, Cande WZ. 2000. Phosphorylation of histone H3 is correlated with changes in the maintenance of sister chromatid cohesion during meiosis in maize, rather than the condensation of the chromatin. *Journal of Cell Science* **113**: 3217–3226.

Kawabe A, Matsunaga S, Nakagawa K, Kurihara D, Yoneda A, Hasezawa S, Uchiyama S, Fukui K. 2005. Characterization of plant Aurora kinases during mitosis. *Plant Molecular Biology* **58**: 1–13.

Kurihara D, Matsunaga S, Kawabe A, Fujimoto S, Noda M, Uchiyama S, Fukui K. 2006. Aurora kinase is required for chromosome segregation in tobacco BY-2 cells. *The Plant Journal* **48**: 572–580.

Kurihara D, Matsunaga S, Uchiyama S, Fukui K. 2008. Live cell imaging reveals plant Aurora kinase has dual roles during mitosis. *Plant and Cell Physiology* **49**: 1256–1261.

Legland D, Arganda-Carreras I, Andrey P. 2016. MorphoLibJ: integrated library and plugins for mathematical morphology with ImageJ. *Bioinformatics* **32**: 3532–3534.

Luger K, Dechassa ML, Tremethick DJ. 2012. New insights into nucleosome and chromatin structure: an ordered state or a disordered affair? *Nature Reviews Molecular Cell Biology* **13**: 436–447.

Manzanero S, Arana P, Puertas MJ, Houben A. 2000. The chromosomal distribution of phosphorylated histone H3 differs between plants and animals at meiosis. *Chromosoma* **109**: 308–317.

Manzanero S, Rutten T, Kotseruba V, Houben A. 2002. Alterations in the distribution of histone H3 phosphorylation in mitotic plant chromosomes in response to cold treatment and the protein phosphatase inhibitor cantharidin. *Chromosome Research* **10**: 467–476.

McManus KJ, Hendzel MJ. 2006. The relationship between histone H3 phosphorylation and acetylation throughout the mammalian cell cycle. *Biochemistry and Cell Biology* **84**: 640–657.

Menges M, Murray JAH. 2002. Synchronous *Arabidopsis* suspension cultures for analysis of cell-cycle gene activity. *The Plant Journal* **30**: 203–212.

Miura K. 2020. Bleach correction ImageJ plugin for compensating the photobleaching of time-lapse sequences. *F1000Research* **9**: 1494.

Sawicka A, Seiser C. 2012. Histone H3 phosphorylation – a versatile chromatin modification for different occasions. *Biochimie* **94**: 2193–2201.

Schaefer E, Belcram K, Uyttewaal M, Duroc Y, Goussot M, Legland D, Laruelle E, De Tauzia-Moreau M-L, Pastuglia M, Bouchez D. 2017. The preprophase band of microtubules controls the robustness of division orientation in plants. *Science* **356**: 186–189.

Schindelin J, Arganda-Carreras I, Frise E, Kaynig V, Longair M, Pietzsch T, Preibisch S, Rueden C, Saalfeld S, Schmid B *et al.* 2012. Fiji: an open-source platform for biological-image analysis. *Nature Methods* **9**: 676–682.

Shi Y. 2009. Serine/threonine phosphatases: mechanism through structure. *Cell* **139**: 468–484.

Spinner L, Gadeyne A, Belcram K, Goussot M, Moison M, Duroc Y, Eeckhout D, De Winne N, Schaefer E, Van De Slijke E *et al.* 2013. A protein phosphatase 2A complex spatially controls plant cell division. *Nature Communications* **4**: 1863.

Talbert PB, Ahmad K, Almouzni G, Ausió J, Berger F, Bhalla PL, Bonner WM, Cande WZ, Chadwick BP, Chan SWL *et al.* 2012. A unified phylogeny-based nomenclature for histone variants. *Epigenetics & Chromatin* **5**: 7.

Tong Y, Ben-Shlomo A, Zhou C, Wawrowsky K, Melmed S. 2008. Pituitary tumor transforming gene 1 regulates Aurora kinase A activity. *Oncogene* **27**: 6385–6395.

Ujvárosi AZ, Riba M, Garda T, Gyémánt G, Vereb G, M-Hamvas M, Vasas G, Máthé C. 2019. Attack of microcystis aeruginosa bloom on a *Ceratophyllum submersum* field: ecotoxicological measurements in real environment with real microcystin exposure. *Science of the Total Environment* **662**: 735–745.

Wang F, Higgins JMG. 2013. Histone modifications and mitosis: countermarks, landmarks, and bookmarks. *Trends in Cell Biology* **23**: 175–184.

Wang J, Tian X, Feng C, Song C, Yu B, Wang Y, Ji X, Zhang X. 2023. Histone H3 phospho-regulation by KimH3 in both interphase and mitosis. *Iscience* **26**: 106372.

Zhang B, Dong Q, Su H, Birchler JA, Han F. 2014. Histone phosphorylation: its role during cell cycle and centromere identity in plants. *Cytogenetic and Genome Research* **143**: 144–149.

Zhou H-W, Nussbaumer C, Chao Y, DeLong A. 2004. Disparate roles for the regulatory A subunit isoforms in Arabidopsis protein phosphatase 2A. *Plant Cell* **16**: 709–722.

Supporting Information

Additional Supporting Information may be found online in the Supporting Information section at the end of the article.

Dataset S1 Values presented in Figs 4, 5c and 6.

Fig. S1 Influence of radius size on particle merging accuracy.

Fig. S2 Comparison of the Bleach Correction and the MCorr methods.

Fig. S3 Behavior of the Attenuation Correction plugin (Biot *et al.*, 2008) on the H3S10ph signal images.

Fig. S4 Neither DAPI nor TO-PRO-3 is a suitable internal control.

Fig. S5 Morphometric analysis of H3S10ph signal according to mitotic stages.

Fig. S6 Graphs plotting the mean integrated density of metaphase H3S10ph objects for the eight roots used for the analysis.

Fig. S7 Influence of the MCorr on the mean integrated density, volume and total integrated density of H3S10ph objects.

Fig. S8 Improved regression fit with the manual correction option of the HisCorrect macro.

Fig. S9 Adjusted *P*-values of the analysis shown in Fig. 6a (a), Fig. 6b (b) and Fig. 6c (c).

Fig. S10 Frequency histograms of prometaphase H3S10ph signals in Col0 (a), *trm678* (b) and *a2/a3* (c) mutants as a function of stack depth.

Methods S1 HisCorrect, HisMeasure and HisAnnot macros tutorial.

Methods S2 HisCorrect macro.

Methods S3 HisMeasure Macro.

Methods S4 HisAnnot Macro.

Please note: Wiley is not responsible for the content or functionality of any Supporting Information supplied by the authors. Any queries (other than missing material) should be directed to the *New Phytologist* Central Office.